Ultrasound in Med. & Biol., Vol. 00, No. 00, pp. 1–8, 2020

0301-5629/$ - see front matter

https://doi.org/10.1016/j.ultrasmedbio.2020.12.007

● *Original Contribution*

ACOUSTIC MEASUREMENTS OF NUCLEUS SIZE DISTRIBUTION AT THE CAVITATION THRESHOLD

Lauren Mancia,* Mauro Rodriguez,† Jonathan R. Sukovich,‡ Scott Haskel,‡ Zhen Xu,‡ and Eric Johnsen*

* Department of Mechanical Engineering, University of Michigan, Ann Arbor, Michigan, USA; † Division of Engineering and Applied Science, California Institute of Technology, Pasadena, California, USA; and ‡ Department of Biomedical Engineering, University of Michigan, Ann Arbor, Michigan, USA

(*Received* 23 *May* 2020; *revised* 1 *October* 2020; *in final from* 10 *December* 2020)

Abstract——An understanding of the acoustic cavitation threshold is essential for minimizing cavitation bio-effects in diagnostic ultrasound and for controlling cavitation-mediated tissue ablation in focused ultrasound procedures. The homogeneous cavitation threshold is an intrinsic material property of recognized importance to biomedical ultrasound as well as a variety of other applications requiring cavitation control. However, measurements of the acoustic cavitation threshold in water differ from those predicted by classic nucleation theories. This persistent discrepancy is explained by combining recently developed methods for acoustically nucleating single bubbles at threshold with numerical modeling to obtain a nucleus size distribution consistent with first-principles estimates for ion-stabilized nuclei. We identify acoustic cavitation at threshold as a reproducible subtype of heterogeneous cavitation with a characteristic nucleus size distribution. Knowledge of the nucleus size distribution could inspire new approaches to achieving cavitation control in water, tissue and a variety of other media. (E-mail: lamancha@umich.edu)

Key Words: **Cavitation, Nucleation, Intrinsic threshold, Bubble dynamics, Histotripsy, Focused ultrasound.**

INTRODUCTION

Predicting the onset of acoustic cavitation is essential for the mitigation and control of cavitation bio-effects in diagnostic ultrasound (Church 2002) and for cavitation control in therapeutic ultrasound procedures (Bader et al. 2019). The population of cavitation nuclei is known to determine the onset of ultrasound-induced cavitation in water (Brotchie et al. 2009; Bader et al. 2019) and tissue (Maxwell et al. 2013; Vlaisavljevich et al. 2014, 2015, 2016) in biomedical ultrasound. The characteristics of cavitation nuclei are of particular interest in histotripsy, a non-thermal focused ultrasound procedure that uses controlled cavitation to homogenize soft tissue into acellular debris (Xu et al. 2005; Parsons et al. 2006; Edsall et al. 2020) for a variety of proposed clinical applications (Khokhlova et al. 2015). Mechanical tissue fractionation in histotripsy requires the creation of a dense cloud of cavitation bubbles at the treatment focus (Xu et al. 2005; Parsons et al. 2007). Given the stochastic nature of cavitation, an understanding of the conditions required for bubble cloud generation and maintenance is important for treatment monitoring and planning (Bader et al. 2019). Furthermore, an understanding of the population of nuclei in the relatively controlled setting of histotripsy treatments provides useful insight into nucleation in other settings. For example, cavitation inception in blast traumatic brain injuries (Salzar et al. 2017) and hydrodynamic applications (Chatterjee and Arakeri 1997) are also thought to involve pre-existing nuclei. Given the stochastic nature of cavitation phenomena, the ability to characterize and potentially control the population of nuclei in a given medium would be useful to all of these applications (Chatterjee and Arakeri 1997; Brotchie et al. 2009; Maxwell et al. 2013). The significance of cavitation nuclei is best appreciated in the context of the cavitation threshold.

Homogeneous cavitation occurs when a medium spontaneously ruptures under a tensile (negative) pressure exceeding its tensile strength (Leighton 2012). Acoustic measurements of the homogeneous cavitation

Address correspondence to: Lauren Mancia, Department of Mechanical Engineering, University of Michigan, 2350 Hayward Street, Ann Arbor, MI 48109, USA. E-mail: lamancha@umich.edu

threshold in water range from −21 to −30 MPa at room temperature (Greenspan and Tschiegg 1982; Herbert et al. 2006; Davitt et al. 2010; Bader et al. 2019) and are of significantly smaller magnitude than values predicted by classic nucleation theory (Debenedetti 1996) and measured using microfluidic techniques (Ando et al. 2012). Self-ionization of water is a proposed source of ion impurities that destabilize water to cavitation (Davitt et al. 2010). Alternatively, these ions could stabilize pre-existing nanoscale gas bubbles against dissolution (Akulichev 1966), producing bubbstons (Bunkin and Bunkin 1992; Sankin and Teslenko 2003). Ion stabilization likely explains the observed longevity of bulk nanobubbles (Uchida et al. 2016; Zhu et al. 2016; Nirmalkar et al. 2018a, 2018b; Fang et al. 2018) and suggests that acoustic methods could be measuring the onset of heterogeneous cavitation in a subpopulation of ion-stabilized, nanoscale nuclei rather than a genuine homogeneous threshold (Sankin and Teslenko 2003; Maxwell et al. 2013). Nevertheless, the reproducibility of acoustic threshold measurements in water of variable purity implies that this subpopulation of nuclei is consistently present of (Borkent et al. 2007; Ando et al. 2012; Maxwell et al. 2013), ubiquitous in water (Davitt et al. 2010; Azouzi et al. 2013) and intrinsic to water and water-based tissues (Bunkin and Bunkin 1992; Bader et al. 2019). Despite their significance to cavitation control, these nuclei remain poorly characterized.

Attempts to use fundamental thermodynamics (Bunkin and Bunkin 1992) or nucleation theories to predict a critical or lower-bound cavitation nucleus size at a given temperature (Davitt et al. 2010; Azouzi et al. 2013) provide limited information on the distribution of nuclei in more practical settings, and failure to account for nucleus size variation within a cloud of acoustically generated bubbles risks neglecting important physics (Wang 1999). Prior work in heterogeneous cavitation suggests that nucleus sizes follow a log-normal (Ben-Yosef et al. 1975; Ando et al. 2011) or Weibull (Wienken et al. 2006) distribution, but it is not clear that these distributions are applicable to nanoscale nuclei present at threshold. Although it is possible to measure the size distributions and other characteristics of nanobubbles (Jin et al. 2007; Bunkin et al. 2014, 2016; Uchida et al. 2016; Zhu et al. 2016; Fang et al. 2018; Nirmalkar et al. 2018a, 2018b), such studies involve methods that nucleate multiple bubbles simultaneously in water that often contains added ions (Jin et al. 2007; Bunkin et al. 2014, 2016; Uchida et al. 2016; Zhu et al. 2016). Though they are likely stabilized by similar physics (Akulichev 1966), these nanobubbles are not necessarily representative of the hypothesized nanoscale nuclei present at the acoustic cavitation threshold in de-ionized water. Moreover, nanoparticle tracking analysis techniques considered most accurate for measuring nanobubble size distributions (Nirmalkar et al. 2018b) have detection limits in the tens of nanometers (Filipe et al. 2010)—larger than estimated sizes for acoustic threshold nuclei (Maxwell et al. 2013; Bader et al. 2019) or for pre-existing bubbstons in very dilute solutions (Bunkin and Bunkin 1992). Finally, previous acoustic methods used to infer threshold nucleus sizes for water and other liquids have also been limited by an inability to track individual bubbles from their points of inception (Sankin and Teslenko 2003; Maxwell et al. 2013). An alternative method adapts homogeneous nucleation theory to the study of acoustic cavitation in water and tissue (Church 2002, 1993). This work assumed spontaneous generation of gas bubbles under energetically favorable conditions and was used to estimate critical nucleus sizes for given sonication conditions. However, all of these methods are limited to inferring a mean or critical nucleus size that gives rise to a single cavitation event at a measured threshold pressure. To date, no study has both distinguished acoustic cavitation at threshold as a highly reproducible subtype of heterogeneous cavitation and provided measured cavitation statistics for the distribution of pre-existing nuclei this implies.

This study presents measurements of nanoscale cavitation nuclei in water, specifically, for the first time, a complete size distribution of nuclei induced to grow at the acoustic cavitation threshold. Our measurements were made by combining a unique ultrasound system capable of producing a single cavitation bubble at threshold (Wilson et al. 2019) with validated numerical modeling (Estrada et al. 2018; Mancia et al. 2020). While liquid water was used in this study, the methods used are general and applicable to transparent tissue-like viscoelastic media (Wilson et al. 2019) and will provide a foundation for future extensions of the method into opaque materials such as tissues.

METHODS

Single-bubble experiments

Single-bubble experiments were previously performed in a study comparing laser-generated cavitation with ultrasound-generated cavitation in water and gels (Wilson et al. 2019), and we leverage the data sets from the water experiments. In brief, water is de-ionized to a resistivity of 18 MΩ, filtered to 2 μm and degassed to 4 kPa. Experiments use a spherical acoustic array containing 16 focused transducer elements with a central frequency of 1 MHz that is capable of generating a single cavitation bubble with a well-characterized pressure waveform. Such control ensures that energy input to

grow the bubble is known for a given nucleus size. Single bubbles are nucleated with a probability of 0.5 using a 1.5-cycle acoustic pulse, which has a single rarefactional pressure half-cycle with a measured (Maxwell et al. 2013) amplitude of −24 MPa. This value is consistent with measurements obtained by our group and others using variable acoustic waveforms and water purity (Herbert et al. 2006; Maxwell et al. 2013; Vlaisavljevich et al. 2016). Images of the bubbles through a single cycle of growth and collapse are obtained using a high-speed camera with a multiflash-per-camera-exposure technique (Sukovich et al. 2020). This technique generates images of nested, concentric bubbles, which are differentiated using brightness thresholding and edge detection. Bubble radii are measured at individual flash points by applying a least-squares circle fit to their detected boundaries. For all experiments, the magnitudes of the spatial and temporal resolution uncertainties are 4.3 μm and <1.25 μs, respectively.

Theoretical model

We simulate the dynamics of a single spherical, homobaric air bubble in water. To account for near-field compressibility effects, radial bubble dynamics are described by the Keller−Miksis equation (Keller and Miksis 1980):

$$\left(1-\frac{\dot{R}}{c_\infty}\right)R\ddot{R}+\frac{3}{2}\left(1-\frac{\dot{R}}{3c_\infty}\right)\dot{R}^2=\frac{1}{\rho_\infty}\left(1+\frac{\dot{R}}{c_\infty}+\frac{R}{c_\infty}\frac{d}{dt}\right)\left[pb-\left(p_\infty+p_f\left(t+\frac{R}{c_\infty}\right)\right)-\frac{2S}{R}-\frac{4\mu\dot{R}}{R}\right] \quad (1)$$

where R is the bubble radius, and c_∞ and p_∞ are the constant sound speed and density of the medium, respectively. The surface tension, S, and viscosity, p, are constants for water at 25°C. The far-field pressure is the sum of the ambient fluid pressure, p_∞, and the acoustic forcing pressure, $P_f(t)$ given in eqn (4). Parameters that remain constant for all simulations are given in Table 1. Equation (2) is solved to determine the internal bubble pressure, $p_b(t)$. The time derivative of p_b couples the Keller−Miksis equation (eqn [1]) to the energy equation for air inside the bubble:

Table 1. Waveform parameters and physical properties held constant for all numerical simulations

Parameter	Value
p_A	−24 MPa
f	1 MHz
n	3.7
δ	5 μs
S	72 mN/m
c_∞	1496 m/s
ρ_∞	1000 kg/m^3
p_∞	101.325 kPa
T_∞	25°C
k	1.4
K_A	5.28×10^{-5} W/mK^2
K_B	1.165×10^{-2} W/mK

$$\dot{p}_b=\frac{3}{R}\left((k-1)K\left.\frac{\partial T}{\partial r}\right|_R-kp_b\dot{R}\right) \quad (2)$$

$$\frac{k}{k-1}\frac{p_b}{T}\left[\frac{\partial T}{\partial t}+\frac{1}{kp_b}\left((k-1)K\frac{\partial T}{\partial r}-\frac{r\dot{p}_b}{3}\right)\frac{\partial T}{\partial r}\right]=\dot{p}_b+\frac{1}{r^2}\frac{\partial}{\partial r}\left(r^2K\frac{\partial T}{\partial r}\right) \quad (3)$$

where $T(r, t)$ is the temperature field of air inside the bubble, which has a ratio of specific heats K. The air has a thermal conductivity given by $K=K_AT+K_B$, where constants K_A and K_B were determined empirically for air (Prosperetti et al. 1988). The initial pressure inside the bubble is $p_b(0)=p_\infty+2S/R$. A boundary condition is prescribed for the center of the bubble: $\nabla T=0$ at $r=0$. The bubble wall boundary condition is $T(R)=T_\infty$ under the assumption that the water remains at its constant ambient temperature through the single cycle of bubble growth and collapse considered in each experiment (Prosperetti 1991; Estrada et al. 2018).

The far-field pressure is the sum of the ambient pressure, p_∞, and time-varying incident pulse, $p_f(t)$:

$$p_f(t)=\begin{cases}p_A\left(\frac{1+\cos[\omega(t-\delta)]}{2}\right)^n, & |t-\delta|\le\frac{\pi}{\omega}\\ 0, & |t-\delta|>\frac{\pi}{\omega}\end{cases} \quad (4)$$

The pressure amplitude, $p_A=-24$ MPa, and frequency, $f=1$ MHz ($\omega=2\pi f$), are approximated from experimental waveform measurements, while the time delay, S = 5 ps, and fitting parameter, n, are chosen as in previous studies (Vlaisavljevich et al. 2014; Mancia et al. 2017). Based on the notion of a cavitation threshold, cavitation occurs only if a sufficiently large tension is applied. The experimental waveform consists of several cycles, and only the peak negative portion is beyond threshold. An analytic approximation of this peak negative pressure portion of a raw experimental waveform (Mancia et al. 2020) is valid in this near-ideal case of inertial cavitation in which the resonant frequency of the bubble is much less than the driving frequency of the waveform.

Numerical methods

The equations are non-dimensionalized (Warnez and Johnsen 2015) using the initial bubble radius, R_0, water density, ρ_∞, equilibrium pressure of the bubble contents, $p_0=p_\infty+2$ S/R, and far-field

temperature, T_∞ to define a characteristic speed, $u_c = \sqrt{p_0/\rho_\infty}$ and dimensionless parameters: Reynolds number, $\mathrm{Re} = \rho_\infty u_c R_0/\mu$, Weber number, $\mathrm{We} = p_0 R_0/2S$, dimensionless sound speed, $C = c_\infty/u_c$, and $\chi = T_\infty K_M/p_0 R_0 u_c$. A variable-step, variable-order solver based on numerical differentiation formulas (MATLAB ODE15s) is used for numerical time marching (Shampine and Reichelt 1997; Shampine et al. 1999). Equations are integrated over a dimensional time span of t = [0,50] in microseconds; results are then time-shifted so that the maximum bubble radius occurs at $t = 0$. By use of numerical methods described by Warnez and Johnsen (2015), the spatial derivatives in the energy equation are discretized on a mesh of $N_s + 1$ points in r-space (Prosperetti et al. 1988) inside the bubble and computed using a spectral collocation method (Warnez and Johnsen 2015). Results are sufficiently converged when simulations use $N_s = 30$ points inside the bubble. The coordinate transformation and characteristic length, $L_v = 3$, were also adopted from Warnez and Johnsen. A more detailed treatment of the derivation and numerical implementation of this model can be found in the literature (Prosperetti et al. 1988; Kamath et al. 1993; Warnez and Johnsen 2015; Barajas and Johnsen 2017).

RESULTS

Aggregate radius-versus-time data sets for 88 acoustically nucleated single-bubble experiments in water degassed to 4 kPa are illustrated in Figure 1a. Although all of the bubbles represented in the curves in Figure 1a were generated under equivalent experimental conditions, significant differences between individual experiments are evident. *Black* points are a single representative data set, and error bars correspond to uncertainty associated with limitations in spatial resolution. Given that most of the other data sets fall outside of these error bars, it can be concluded that error associated with limitations in spatial resolution does not explain the data spread. Figure 1b illustrates that the data sets collapse when scaled by the measured maximum radius and collapse time, $t_c = 0.92R\sqrt{\rho/P_\infty}_{\max}$ where R_{max} is the maximum bubble radius of a given data set, ρ_∞ is liquid density, and p_∞ is the far-field liquid pressure (both constants given in Table 1). Thus, all experiments are governed by the same physics with exceedingly small uncertainty once appropriate scaling addresses uncertainties in initial conditions. In particular, the energy delivered by the ultrasound pulse to the nucleus grows the bubble as the bubble expands to maximum radius against its surroundings. That initial energy is proportional to the nucleus volume and ultrasound pressure amplitude. Given the negligible error in pressure amplitude measurement and its consistency with previous studies (Davitt et al. 2010), we hypothesize that the data spread is owing to different nanoscale nucleus sizes corresponding to each experiment. Validated numerical methods can then be used in combination with experimental data to infer these unknown nucleus sizes.

To construct the nucleus size distribution, we hypothesize that cavitation nuclei exist as stabilized nanobubbles (Sankin and Teslenko 2003; Maxwell et al. 2013) and seek to determine the minimum

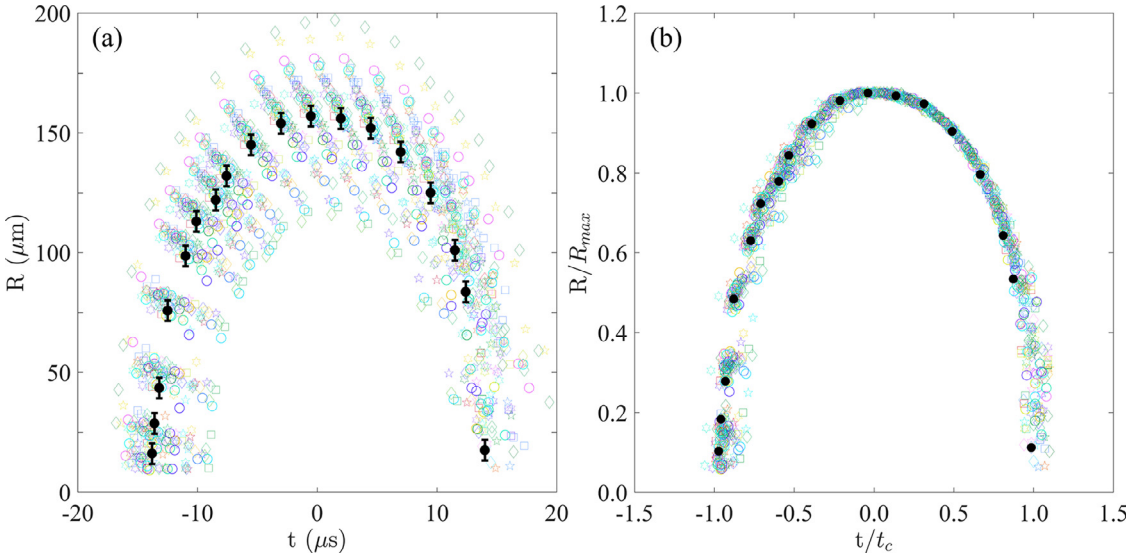

Fig. 1. (a) Radius-versus-time measurements from 88 experiments in water degassed to 4 kPa. Clustering of data sets is a consequence of aligning all data such that the maximum radii occur at $t = 0$. A single data set is shown in *black* with spatial resolution error bars. (b) Data sets scaled by maximum radius and collapse time.

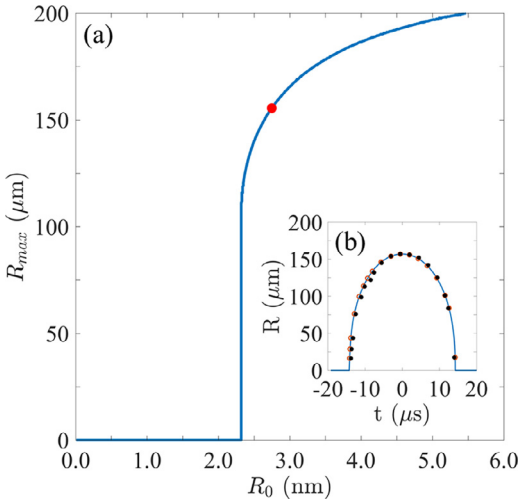

Fig. 2. (a) Simulation R_{max} versus nucleus size. (b) Representative data set in black. The simulation (*blue trace*) initialized with R_0 indicated by the *solid red point* in (a) optimizes the normalized root-mean-squared error between experiment and simulation nearest neighbors (*red open points*).

nucleus size, R_0^*, required for cavitation growth at a given threshold pressure. Based on past work on the acoustic cavitation threshold (Maxwell et al. 2013; Vlaisavljevich et al. 2015, 2016), the threshold pressure is fixed at its measured value of −24 MPa for all simulations. Figure 2a illustrates the simulation maximum bubble radius as a function of nucleus size under this tensile pressure. Bubble growth is negligible until a minimum nucleus size of $R_0^* = 2.32$ nm is reached.

The complete nucleus size distribution is created by varying the R_0 used to initialize simulations over the range 2.32−6.00 nm for each experimental data set. A nearest-neighbors algorithm with a standardized Euclidean distance metric is then used to identify simulation points closest to experimental data points. The nucleus distribution consists of R_0 values that optimize the normalized root-mean-squared (rms) error between experimental data points and their simulation nearest neighbors. The average normalized rms error for these data sets is 0.98 (with 1.00 implying a perfect fit). Figure 2b illustrates the representative data set from Figure 1. The simulation initialized with $R_0 = 2.78$ nm (indicated by the *red point* in Fig. 2a) optimizes the normalized rms error between the experimental data (*black points*) and the nearest neighbors on the simulation trace (*red open points*). This procedure is followed for each data set to obtain the R_0 distribution.

Simulations initialized with different nucleus sizes effectively bound the experimental data sets, as illustrated in Figure 3. Aggregate experimental data from Figure 1 are in *black*, and the *shaded region* is bounded by simulations initialized with the smallest nucleus size,

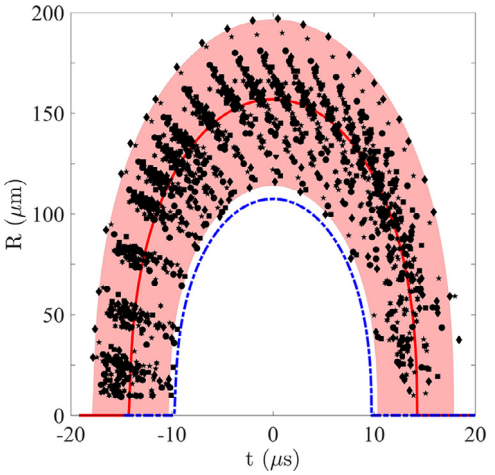

Fig. 3. Experimental data from Figure 1. The *shaded region* is bounded by simulations initialized with the smallest and largest nuclei. The *dark red trace* is the simulation corresponding to the mean nucleus size. The *dashed blue trace* is the simulation initialized with R_0^*.

$R_0 = 2.33$ nm, and the largest nucleus size, $R_0 = 4.99$ nm, that optimize the normalized rms error. The *dark red trace* is the simulation initialized with the mean nucleus size of 2.88 nm, and the *blue dashed trace* is the simulation initialized with the predetermined, lower-bound nucleus, $R_0^* = 2.32$ nm. The nucleus size distribution is best approximated by a log-normal probability distribution function (PDF), outlined in *red* in Figure 4, which has $\sigma = 0.11$ and $\mu = 1.0$. This finding is consistent with previous use of a log-normal distribution to model equilibrium bubble sizes for polydisperse flow based on measured bubble populations in a water tunnel and ocean water (Ben-Yosef et al. 1975; Ando et al. 2011).

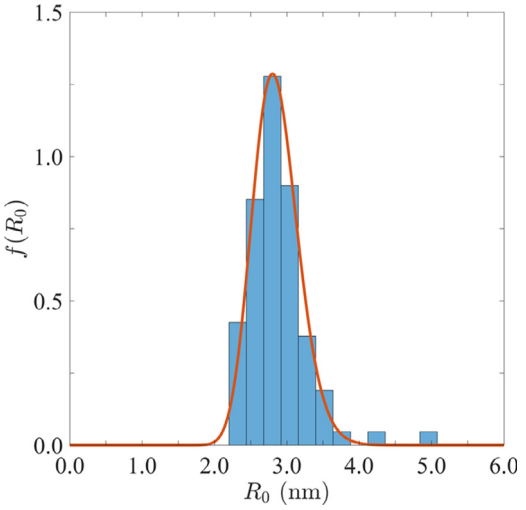

Fig. 4. Nucleus size distribution fitted to log-normal probability distribution function (*red*).

DISCUSSION

The nucleus size distribution is consistent with previous studies that estimated the sizes of ion-stabilized nuclei to be between 2 and 4 nm (Bunkin and Bunkin 1992; Sankin and Teslenko 2003), and supports the hypothesis that hydronium ions (*e.g.,* those produced during self-ionization of water) are the ubiquitous impurity responsible for the discrepancy between acoustically measured and theoretical homogeneous cavitation thresholds (Davitt et al. 2010). The log-normal PDF parallels size distributions measured for larger cavitation bubbles in settings of heterogeneous cavitation (Ben-Yosef et al. 1975; Ando et al. 2011), and nuclei measured in this study are at least 1 nm larger than those obtained using homogeneous nucleation theories. These findings suggest that acoustic methods, even in highly purified water, are measuring a threshold for heterogeneous rather than homogeneous cavitation. However, consistency in measurements (Greenspan and Tschiegg 1982; Herbert et al. 2006; Davitt et al. 2010) distinguishes cavitation at the acoustic threshold as a reflection of the nuclei population intrinsic to that medium.

Despite significant differences in waveform and water quality used in previous experiments (Herbert et al. 2006; Maxwell et al. 2013), measured acoustic cavitation thresholds differ from each other and from ours by <4 MPa. A previous study also notes that their threshold measurements are stable even to the deliberate introduction of impurities (Herbert et al. 2006). However, there is evidence that gas concentration of the water could give rise to larger nuclei (Akulichev 1966). Although more data are required to verify the relationship between dissolved gas concentration and nucleus size, experiments performed in water degassed to 40 kPa (~40% air saturation) instead of to the original 4 kPa (~ 4% air saturation) (Wilson et al. 2019) indicate that the higher gas content has a negligible effect on the measured acoustic cavitation threshold of −24 MPa. From 28 single-bubble experimental data sets, we infer a mean nucleus size of 3.60 nm, with nucleus sizes ranging from 2.64−5.78 nm. Thus, slightly larger nuclei are measured, as expected from the arguments presented in Akulichev (1966), but the mean nucleus sizes agree to within <1 nm despite the 10-fold difference in gas content of the water. Though more in-depth studies of the matter would be beneficial, the present results support previous findings that the acoustic cavitation threshold is relatively stable to changes in air saturation in the liquid.

Our method for determining the nucleus size distribution infers quantities well below the resolution limits of experiments, but our theory could be strengthened by greater consideration of nanoscale physics. For example, ion interactions could affect the earliest stages of bubble growth when nucleus sizes are nanoscopic. Additionally, nucleation phenomena are highly dependent on surface tension (Church 2002), and the effective surface tension experienced by a nanoscale nucleus differs from that of the bulk medium (Azouzi et al. 2013). Investigation of these effects will be the subject of future work, with molecular dynamics simulations offering the most robust approach. Finally, our work has focused on water given its well-characterized physical properties and an acoustic cavitation threshold that is comparable to that of water-based soft tissues (Maxwell et al. 2013; Bader et al. 2019). However, our method is general and, with modifications, can be applied to other liquids and viscoelastic media exhibiting thresholds outside of the typical range for water and water-based tissues (Maxwell et al. 2013).

Determination of lower-bound nucleus size

Bubble growth is negligible until a minimum nucleus size is reached, and Figure 2a indicates a minimum nucleus size of $R_0^* = 2.32$ nm for the present problem. To efficiently obtain the complete nucleus size distribution, it is valuable to know this lower-bound nucleus size before simulations are performed. The duration of the tensile pulse is much longer than the resonant period of the bubble, so the quasistatic assumption holds. This allows one to calculate the minimum nucleus size using the Blake threshold concept (Leighton 2012). The minimum pressure amplitude needed to cause explosive growth of a bubble with initial radius R_0 is given by

$$p_B = p_\infty + \frac{8S}{9}\sqrt{\frac{3S}{2(p_0 + 2S/R_0)R_0^3}} \tag{5}$$

where p_B is the Blake threshold. Assuming $2S/R_0 >> p_0$ for these nanoscale nuclei gives rise to a simplified expression for R_0:

$$R_0 = \frac{4S}{3\sqrt{3}}\left(\frac{1}{p_B - p_\infty}\right) \tag{6}$$

In the present case, the Blake threshold pressure is equivalent to the measured threshold pressure: $p_B = 24$ MPa. Substituting the other physical constants into eqn (6) yields $R_0 = 2.32$ nm $= R_0^*$, which is the minimum bubble radius that will grow when exposed to the measured Blake threshold pressure (Walton and Reynolds 1984). For comparison, previous studies estimate the minimum radii of stabilized nanoscale nuclei to be approximately 2.0 nm (Bunkin and Bunkin 1992) from first principles and 2.5 nm (Maxwell et al. 2013) from bubble dynamics simulations. In contrast, critical nucleus volumes obtained using homogeneous nucleation theories

correspond to radii of 1.3 nm (Davitt et al. 2010) and 0.88 nm (Azouzi et al. 2013) at 300 K.

Finally, it is worth noting that eqn (6) is consistent with a previously noted inverse relationship between cavitation threshold and nucleus size (Vlaisavljevich et al. 2015). In a practical sense, however, the cavitation threshold is a measured quantity that is intrinsic to the experimental water sample. The nucleation of single bubbles at a defined threshold rate of 50% is contingent on a controlled peak negative pressure of 24 MPa, which has negligible experimental error and so is fixed in all simulations and for the minimum nucleus size analysis. To predict an analogous cavitation threshold from a nucleus size distribution, one must know the minimum nucleus size induced to cavitate at this rate in the relevant water sample.

CONCLUSIONS

In summary, this work presents a new approach to using single-bubble experiments and numerical simulations to measure the size distribution of nanoscale cavitation nuclei present at the acoustic cavitation threshold. Recognizing that the leading-order experimental uncertainty lies in the initial population of nuclei, the inverse problem for the nucleus size distribution is solved with a single-bubble numerical model. The nucleus size distribution obeys a log-normal PDF ranging from 2.33 to 4.99 nm with a mean of 2.88 nm. Although water is the only medium considered in this study, the methods presented here could be readily extended to predict the intrinsic nucleus size distributions characteristic of other liquids and tissue-like media, thus offering a new avenue for achieving cavitation control in biomedical ultrasound and a variety of other applications.

Acknowledgments—This work was supported by Office of Naval Research Grant No. N00014-18-1-2625 (under Dr. Timothy Bentley).

Conflict of interest disclosure—Z.X. has financial interests and/or other relationship with HistoSonics Inc.

REFERENCES

Akulichev V. Hydration of ions and the cavitation resistance of water. Acoust Phys 1966;12:144–150.

Ando K, Colonius T, Brennen CE. Numerical simulation of shock propagation in a polydisperse bubbly liquid. Int J Multiphase Flow 2011;37:596–608.

Ando K, Liu AQ, Ohl CD. Homogeneous nucleation in water in microfluidic channels. Phys Rev Lett 2012;109 044501.

Azouzi MEM, Ramboz C, Lenain JF, Caupin F. A coherent picture of water at extreme negative pressure. Nat Phys 2013;9:38.

Bader KB, Vlaisavljevich E, Maxwell AD. For whom the bubble grows: Physical principles of bubble nucleation and dynamics in histotripsy ultrasound therapy. Ultrasound Med Biol 2019;45:1056–1080.

Barajas C, Johnsen E. The effects of heat and mass diffusion on freely oscillating bubbles in a viscoelastic, tissue-like medium. J Acoust Soc Am 2017;141:908–918.

Ben-Yosef N, Ginio O, Mahlab D, Weitz A. Bubble size distribution measurement by Doppler velocimeter. J Appl Phys 1975;46:738–740.

Borkent BM, Arora M, Ohl CD. Reproducible cavitation activity in water–particle suspensions. J Acoust Soc Am 2007;121:1406–1412.

Brotchie A, Grieser F, Ashokkumar M. Effect of power and frequency on bubble-size distributions in acoustic cavitation. Phys Rev Lett 2009;102 084302.

Bunkin N, Bunkin F. Bubbstons: Stable microscopic gas bubbles in very dilute electrolytic solutions. J Exp Theor Phys 1992;74:271–276.

Bunkin NF, Shkirin AV, Burkhanov IS, Chaikov LL, Lomkova AK. Study of the nanobubble phase of aqueous NaCl solutions by dynamic light scattering. Quantum Electron 2014;44:1022.

Bunkin NF, Shkirin AV, Suyazov NV, Babenko VA, Sychev AA, Penkov NV, Belosludtsev KN, Gudkov SV. Formation and dynamics of ion-stabilized gas nanobubble phase in the bulk of aqueous NaCl solutions. J Phys Chem B 2016;120:1291–1303.

Chatterjee D, Arakeri VH. Towards the concept of hydrodynamic cavitation control. J Fluid Mech 1997;332:377–394.

Church CC. An alternative to the mechanical index as a means of assessing the safety of exposures to diagnostic ultrasound. J Acoust Soc Am 1993;93:2348. –2348.

Church CC. Spontaneous homogeneous nucleation, inertial cavitation and the safety of diagnostic ultrasound. Ultrasound Med Biol 2002;28:1349–1364.

Davitt K, Arvengas A, Caupin F. Water at the cavitation limit: Density of the metastable liquid and size of the critical bubble. EPL 2010;90:16002.

Debenedetti PG. Metastable liquids: Concepts and principles. Princeton, NJ: Princeton University Press; 1996.

Edsall C, Khan ZM, Mancia L, Hall S, Mustafa W, Johnsen E, Klibanov AL, Durmaz YY and Vlaisavljevich E, 2020. Bubble Cloud Behavior and Ablation Capacity for Histotripsy Generated from Intrinsic or Artificial Cavitation Nuclei. Ultrasound in Medicine & Biology.

Estrada JB, Barajas C, Henann DL, Johnsen E, Franck C. High strain-rate soft material characterization via inertial cavitation. J Mech Phys Solids 2018;112:291–317.

Fang Z, Wang L, Wang X, Zhou L, Wang S, Zou Z, Tai R, Zhang L, Hu J. Formation and stability of surface/bulk nanobubbles produced by decompression at lower gas concentration. J Phys Chem C 2018;122:22418–22423.

Filipe V, Hawe A, Jiskoot W. Critical evaluation of nanoparticle tracking analysis (NTA) by nanosight for the measurement of nanoparticles and protein aggregates. Pharm Res 2010;27:796–810.

Greenspan M, Tschiegg CE. Radiation-induced acoustic cavitation; threshold versus temperature for some liquids. J Acoust Soc Am 1982;72:1327–1331.

Herbert E, Balibar S, Caupin F. Cavitation pressure in water. Phys Rev E 2006;74 041603.

Jin F, Li J, Ye X, Wu C. Effects of pH and ionic strength on the stability of nanobubbles in aqueous solutions of α-cyclodextrin. J Phys Chem B 2007;111:11745–11749.

Kamath V, Prosperetti A, Egolfopoulos F. A theoretical study of sonoluminescence. J Acoust Soc Am 1993;94:248–260.

Keller JB, Miksis M. Bubble oscillations of large amplitude. J Acoust Soc Am 1980;68:628–633.

Khokhlova VA, Fowlkes JB, Roberts WW, Schade GR, Xu Z, Khokhlova TD, Hall TL, Maxwell AD, Wang YN, Cain CA. Histotripsy methods in mechanical disintegration of tissue: Towards clinical applications. Int J Hyperthermia 2015;31:145–162.

Leighton T. The acoustic bubble. San Diego: Academic Press; 2012.

Mancia L, Rodriguez M, Sukovich J, Xu Z and Johnsen E, 2020. Single-bubble dynamics in histotripsy and high-amplitude ultrasound: Modeling and validation. Physics in Medicine & Biology, 65(22), p.225014.

Mancia L, Vlaisavljevich E, Xu Z, Johnsen E. Predicting tissue susceptibility to mechanical cavitation damage in therapeutic ultrasound. Ultrasound Med Biol 2017;43:1421–1440.

Mancia L, Vlaisavljevich E, Yousefi N, Rodriguez M, Ziemlewicz TJ, Lee FT, Henann D, Franck C, Xu Z, Johnsen E. Modeling tissue-selective cavitation damage. Phys Med Biol 2019;64 225001.

Maxwell AD, Cain CA, Hall TL, Fowlkes JB, Xu Z. Probability of cavitation for single ultrasound pulses applied to tissues and tissue-mimicking materials. Ultrasound Med Biol 2013;39:449–465.

Nirmalkar N, Pacek A, Barigou M. Interpreting the interfacial and colloidal stability of bulk nanobubbles. Soft Matter 2018a;14:9643–9656.

Nirmalkar N, Pacek A, Barigou M. On the existence and stability of bulk nanobubbles. Langmuir 2018b;34:10964–10973.

Parsons JE, Cain CA, Abrams GD, Fowlkes JB. Pulsed cavitational ultrasound therapy for controlled tissue homogenization. Ultrasound Med Biol 2006;32:115–129.

Parsons JE, Cain CA, Fowlkes JB. Spatial variability in acoustic backscatter as an indicator of tissue homogenate production in pulsed cavitational ultrasound therapy. IEEE Trans Ultrason Ferroelectr Freq Control 2007;54:576–590.

Prosperetti A. The thermal behaviour of oscillating gas bubbles. J Fluid Mech 1991;222:587–616.

Prosperetti A, Crum LA, Commander KW. Nonlinear bubble dynamics. J Acoust Soc Am 1988;83:502–514.

Salzar RS, Treichler D, Wardlaw A, Weiss G, Goeller J. Experimental investigation of cavitation as a possible damage mechanism in blast-induced traumatic brain injury in post-mortem human subject heads. J Neurotrauma 2017;34:1589–1602.

Sankin G, Teslenko V. Two-threshold cavitation regime. Dokl Phys 2003;48:665–668.

Shampine LF, Reichelt MW. The MATLAB Ode suite. SIAM J Sci Comput 1997;18:1–22.

Shampine LF, Reichelt MW, Kierzenka JA. Solving index-1 DAEs in MATLAB and simulink. SIAM Rev 1999;41:538–552.

Sukovich JR, Haskell SC, Xu Z, Hall TL. A cost-effective, multi-flash, ghost imaging technique for high temporal and spatial resolution imaging of cavitation using still-frame cameras. J Acoust Soc Am 2020;147:1339–1343.

Uchida T, Liu S, Enari M, Oshita S, Yamazaki K, Gohara K. Effect of NaCl on the lifetime of micro- and nanobubbles. Nanomaterials 2016;6:31.

Vlaisavljevich E, Maxwell A, Warnez M, Johnsen E, Cain C, Xu Z. Histotripsy-induced cavitation cloud initiation thresholds in tissues of different mechanical properties. IEEE Trans Ultrason Ferroelectr Freq Control 2014;61:341–352.

Vlaisavljevich E, Lin KW, Maxwell A, Warnez MT, Mancia L, Singh R, Putnam AJ, Fowlkes B, Johnsen E, Cain C, Xu Z. Effects of ultrasound frequency and tissue stiffness on the histotripsy intrinsic threshold for cavitation. Ultrasound Med Biol 2015;41:1651–1667.

Vlaisavljevich E, Xu Z, Maxwell AD, Mancia L, Zhang X, Lin KW, Duryea AP, Sukovich JR, Hall TL, Johnsen E, Cain C. Effects of temperature on the histotripsy intrinsic threshold for cavitation. IEEE Trans Ultrason Ferroelectr Freq Control 2016;63:1064–1077.

Walton AJ, Reynolds GT. Sonoluminescence. Adv Phys 1984;33:595–660.

Wang YC. Effects of nuclei size distribution on the dynamics of a spherical cloud of cavitation bubbles. J Fluids Eng 1999;121:881–886.

Warnez M, Johnsen E. Numerical modeling of bubble dynamics in viscoelastic media with relaxation. Phys Fluids 2015;27 063103.

Wienken W, Stiller J, Keller A. A method to predict cavitation inception using large-eddy simulation and its application to the flow past a square cylinder. J Fluids Eng 2006;128:316–325.

Wilson CT, Hall TL, Johnsen E, Mancia L, Rodriguez M, Lundt JE, Colonius T, Henann DL, Franck C, Xu Z, Sukovich JR. Comparative study of the dynamics of laser and acoustically generated bubbles in viscoelastic media. Phys Rev E 2019;99 043103.

Xu Z, Fowlkes JB, Rothman ED, Levin AM, Cain CA. Controlled ultrasound tissue erosion: The role of dynamic interaction between insonation and microbubble activity. J Am Acoust Soc Am 2005;117:424–435.

Zhu J, An H, Alheshibri M, Liu L, Terpstra PM, Liu G, Craig VS. Cleaning with bulk nanobubbles. Langmuir 2016;32:11203–11211.